2022-01-1039 Published 30 Aug 2022

An Investigation into the Effects of Swirl on the Performance and Emissions of an Opposed-Piston Two-Stroke Engine using Large Eddy Simulations

Patrick Christopher O'Donnell, Brian Gainey, Erik Vorwerk, Robert Prucka, and Benjamin Lawler
Clemson University

Ming Huo and Ashwin Salvi Achates Power Inc

Citation: O'Donnell, P.C., Gainey, B., Vorwerk, E., Prucka, R. et al., "An Investigation into the Effects of Swirl on the Performance and Emissions of an Opposed-Piston Two-Stroke Engine using Large Eddy Simulations," SAE Technical Paper 2022-01-1039, 2022, doi:10.4271/2022-01-1039.

Received: 29 Apr 2022 Revised: 01 Jun 2022 Accepted: 05 Jul 2022

Abstract

Opposed-piston two-stroke (OP-2S) engines have the potential to achieve higher thermal efficiency than a conventional four-stroke diesel engine. However, the uniflow scavenging process is difficult to control over a wider range of speed and loads due to its sensitivity to pressure dynamics, port timings, and port design. Specifically, the angle of the intake ports can be used to generate swirl which has implications for open and closed cycle effects. This study proposes an analysis of the effects of port angle on the in-cylinder flow distribution and combustion performance of an OP-2S using computational fluid dynamics engine. Large Eddy Simulation (LES) was used to model turbulence given its ability to predict in-cylinder mixing and cyclic variability. A three-cylinder model was validated to experimental data collected by Achates Power and the grid was verified using an LES quality approach from the literature. The model was used to simulate port angles from 12 to 29 degrees at constant pressure and temperature boundary conditions. Results indicated that the higher bulk swirl ratio generated by larger port angles tends to trap more internal residuals. This effect on the scavenging performance, combined with the larger trapped swirl ratio, also has a significant impact on the combustion performance in a two-stroke engine. It was concluded that there exists a tradeoff of efficiency and emissions that must be considered when increasing the port angle in a uniflow two-stroke engine.

1. Introduction

Two-stroke engines were developed in the 1800s and are commonly used in practice today for lightweight power applications such as motorcycles or handheld power tools, as well as large-bore low speed engines for stationary power and marine applications. Two-stroke engines provide the distinct advantage of higher torque/power output but present challenges due to its coupled intake and exhaust process. Four-stroke engines have the benefit of using two full piston strokes to induct intake charge and to expel exhaust gases. Controlling the trapped charge composition in a two-stroke engine via a scavenging process is crucial for reliable and efficient engine operation.

Scavenging in a two-stroke engine is typically classified by how the intake and exhaust ports are positioned in the combustion chamber and there are three conventional types: loop scavenging, crossflow scavenging, and uniflow scavenging [1]. Both loop and crossflow scavenging direct intake flow upwards through the combustion chamber but differ in the positioning of the exhaust ports [2, 3, 4, 5, 6, 7, 8, 9]. These scavenging approaches are limited by the need for a complex combustion chamber design to accommodate the desired flow path and generally result in lower scavenging performance compared to that of uniflow scavenging. In a uniflow scavenging process, fresh charge is forced through one end of the combustion chamber and flows axially towards the other end, forcing hot residuals along with it [10, 11, 12]. It has been shown in previous work that uniflow scavenging is the most efficient at removing exhaust gases with minimal short-circuited mass (i.e., fresh charge exiting the exhaust ports) [13, 14]. A unique design that takes advantage of this scavenging strategy is an opposed-piston two -stroke (OP-2S) engine. OP-2S engines position two pistons on opposing ends of the combustion chamber that act to reveal two sets of ports

(intake and exhaust) that are uniformly located around the circumference acting to reduce flow bias in the cylinder. This engine design has historically faced challenges associated with emissions and durability but still possesses inherent benefits that make it a desirable candidate for future applications [15, 16, 17].

Several characteristics of the OP-2S engines result in its potential to achieve high thermal efficiency and reduced emissions compared to that of a four-stroke engine [18, 19, 20, 21, 22]. First, the use of two opposed pistons enables larger stroke-to-bore ratios which reduce heat loss to the combustion chamber due to smaller surface area to volume ratios. Additionally, achieving the same power output with this design is possible with fewer cylinders than that of a typical four-stroke engine. Also, some mechanical parts needed for four-stroke operation, like camshafts and poppet valves, are not needed in an OP-2S which improves mechanical efficiency and reduces manufacturing cost. However, the scavenging process of the OP-2S engine requires further investigation. Additionally, each piston experiences high thermal loads with less time for cooling between combustion events (i.e., one combustion event every crank rotation as opposed to every other crank rotation for a four-stroke engine). Finally, the injectors must be side mounted in the cylinder liner which poses difficulties in fuel spray mixing and distribution. Recent work on OP-2S engines by Achates Power has found success mitigating these challenges to achieve high power outputs but further work is needed to understand this architecture to continue to advance this engine design [18, 19, 20, 21, 22].

An approach to understanding the complex flow behavior and patterns in uniflow-scavenged two-stroke engines is three-dimensional (3D) computational fluid dynamics (CFD) simulations. 3D-CFD can simulate the fluid flow through the entire engine geometry but has been limited by its heavy computational expense in the past. With the rapid advancement of computing power over the last 20 years, this computational expense is less of limitation. One of the main challenges that is still prevalent with CFD is accurate modeling of turbulence. Direct solution to the governing equations where all length and time scales are resolved, commonly known as Direct Numerical Simulation (DNS), is still impractical for engine applications. There exists a need to accurately predict the fluctuations and instabilities in the flow and one method to do so is Reynold's Averaged Navier Stokes (RANS). RANS models use a time-averaging condition that models all length and time scales and, as a result, are very dissipative [23]. These models incur minimal computational expense and are effective at achieving mean flow solutions for most engineering applications. Large Eddy Simulations (LES) are another class of turbulence models that aim to solve only the large, energy-containing eddies and model the smaller scales. LES models are less dissipative than RANS but require denser computational grids and thus, greater computational cost. But LES models have been proven to provide distinct advantages over RANS models including increased design sensitivity and better prediction of flow structures [24, 25, 26, 27]. For these reasons, the application of LES to internal combustion engines enables the study of cyclic variability and better prediction of in-cylinder mixing which are both relevant to the study of OP-2S engines.

This current study proposes the use of 3D-CFD with LES turbulence modeling, detailed chemistry, and spray modeling to accurately simulate the conditions encountered in an OP-2S engine. A three-cylinder computational model was developed and previously validated using experimental data collected by Redon et al. [19, 28]. A subset of this model that isolated one cylinder was simulated using cycle-averaged and cylinder-averaged initial and boundary conditions from the three-cylinder model. This new one-cylinder model enabled the use of finer grids that are necessary for accurate and resolved LES simulations. For this study, the one-cylinder was used to simulate five port designs with varying port angles (defined in Section 3) ranging from 12 degrees to 29 degrees to investigate the impact of this parameter on closed-cycle performance. Each port design was simulated for ten consecutive two-stroke engine cycles until the ensemble mean for trapped conditions and performance reached steady-state. This sweep of port angle provided insight into the effect of swirl ratio on the overall combustion performance as well as the formation of NOx and soot emissions. It also provided indications for potential areas of improvement related to the optimization of the diesel spray injection. The complex flow phenomena and the combustion process are visualized through the use of cut planes and joint probability density functions.

2. Computational Model

A prototype three-cylinder OP2S engine was modeled in CAD for computational purposes. A numerical model of this engine design was developed using CONVERGE CFD software [29, 30]. Table 1 lists the specifications of the engine. More details about the experimental setup can be found in Redon et al. [18, 19]. Experimental data was collected by Achates Power on this engine, achieving a brake thermal efficiency (BTE) of 42.1% and a brake specific fuel consumption (BSFC) of 199 g/kWh at a load of 13.4 bar and 1600 rpm [19]. This experimental operating condition was used for validation of the computational model. It should be noted that the term minimum volume (MV) is used instead of top dead center (TDC). OP-2S designs require a crank lead between intake and exhaust pistons to avoid interference at each TDC. The

TABLE 1 Engine specifications of the Achates Power OP-2S engine

Bore	98.43 mm
Stroke per Piston	110 mm
Total Stroke	220 mm
Connecting Rod Length	258 mm
Engine Speed	1600 rpm
Net IMEP	13.4 bar
Exhaust Gas Recirculated Fraction [%]	19.6%
Fuel	Diesel
Intake Opening / Closing	127.0 / -119.0 crank angle degrees (CAD) after minimum volume (aMV)
Exhaust Opening / Closing	112.5 / -120.5 CAD aMV

FIGURE 1 Comparison of computational models used in this study and previous work: (a) three-cylinder model of the physical engine, (b) one-cylinder model extracted from three-cylinder model to study open-cycle performance (previous work), and (c) same one-cylinder model with portion of exhaust chest included.

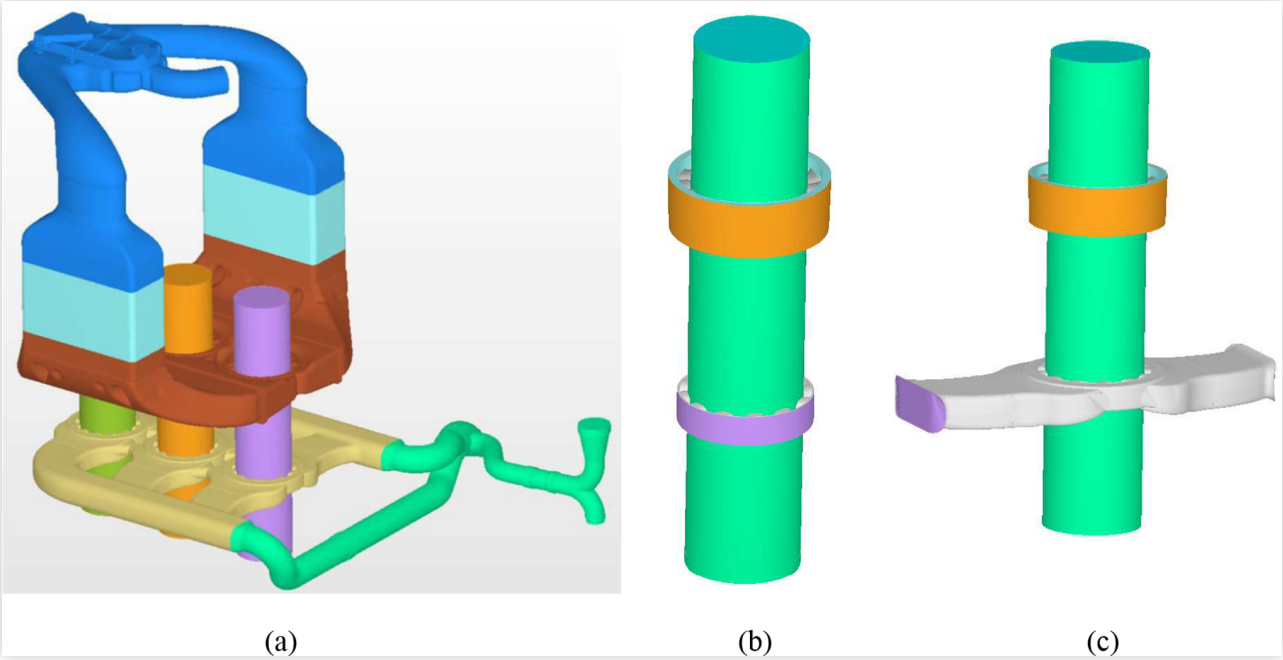

minimum volume occurs at some point between each piston's top dead center position.

Previous work done by the authors simulated this three-cylinder OP-2S engine for fifteen consecutive engine cycles until a quasi-steady state was reached and then validated the model at the experimental conditions mentioned previously. This work also validated the accuracy of the approach to extract one cylinder and simulate it for one breathing stroke to study the effects of intake port design on open-cycle scavenging [28]. In this study, one-cylinder was extracted in a similar manner but included a larger portion of the exhaust chest and was simulated for full engine cycles. A larger portion of the exhaust chest was included to better understand predictions of exhaust composition and heat transfer. Figure 1 compares the models mentioned: (a) three-cylinder model, (b) one-cylinder model used in previous study, and (c) current one-cylinder model. The subsequent sections describe the details of the computational scheme used for the current one-cylinder model and illustrate how the data from the three-cylinder model are utilized. More details about the computational scheme for the three-cylinder model can be found in [28].

2.1. Physical Modeling

The equation of state used to predict non-ideal gas behavior was Reidlich-Kwong [31]. Favre (density-weighted) averaging was used throughout the governing equations. Additionally, the Pressure Implicit with Splitting of Operator (PISO) algorithm was used to solve the pressure-velocity coupling [32, 33]. Additionally, a variable time-stepping algorithm was employed using maximum Courant-Friedrichs-Lewy (CFL) numbers for convection, diffusion, and Mach number of 1, 2, and 50, respectively. These values were held constant throughout the simulations. The following subsections describe additional aspects of the computational model in more detail.

2.1.1. Turbulence Modeling Turbulence was modeled using a 1-equation Large Eddy Simulation (LES) model [24, 29, 30]. LES employs a space-averaging (filtering) approach that decomposes flow variables (θ_i) into a filtered, resolvable scale component ($\overline{\theta_i}$) and a sub-grid scale component (θ_i'). LES turbulence models differ from Reynolds Average Navier Stokes (RANS) models, which model all length and time scales to achieve a time-averaged solution, in that the large, energy-containing eddies are resolved. The Dynamic Structure LES model balances the flow of energy between the resolvable and sub-grid scales by including a transport equation for the sub-grid kinetic energy, given in tensor form by Equation 1 [29, 30]. The sub-grid stress tensors (τ_{ij}) are modeled as a function of the sub-grid scale turbulent kinetic energy (k), shown in Equation 2 [29, 30].

$$\frac{\partial k}{\partial t} + \overline{u_t}\frac{\partial k}{\partial x_i} = -\tau_{ij}\frac{\partial \overline{u_t}}{\partial x_j} - \varepsilon + \frac{\partial}{\partial x_i}\left(\frac{\nu_t}{\sigma_k}\frac{\partial k}{\partial x_i}\right) \quad (1)$$

$$\tau_{ij} = c_{ij}k \quad (2)$$

2.1.2. Spray Modeling The complex flow phenomena and fluid conditions present challenges in modeling a liquid spray injection process. Therefore, various sub-models are necessary to attain accurate results. The Kelvin-Helmholtz/

Rayleigh-Taylor (KH-RT) model was used to model spray penetration, breakup, and atomization [34, 35, 36, 37]. A correlation for droplet evaporation that predicts the time rate of change of droplet size based on the liquid diffusivity and vapor mass fraction was implemented [34]. The effects of turbulence on the dispersion of liquid droplets were modeled using the O'Rourke model, which assumes that the components of the fluid phase velocity have a Gaussian distribution [34]. A model for spray-wall interaction was used which includes a wall film coupled with the film splash model developed by O'Rourke [34, 35, 36, 37]. Droplet collision and drop drag were modeled using the No Time Counter (NTC) model and the Dynamic Drop Drag model developed by Liu et al., respectively [38, 39].

The distribution of the droplet sizes was assigned according to the Blob Injection model where the sizes are equal to the effective diameter [36]. A discharge coefficient that reduces the effective diameter of the injected droplets was determined via experimental analysis of the engine to be 0.8. An additional velocity coefficient model was used to control the velocity of the injected droplets dynamically [37].

2.1.3. Combustion/Emissions Modeling

The non-premixed (diesel-style diffusion) combustion process was modeled with the SAGE detailed chemistry solver developed by Senecal et al. with adaptive zoning for fuel fraction and temperature [40, 41, 42]. Chemical kinetics was predicted using a modified version of Chalmer's n-heptane mechanism for better NOx prediction [43]. All emissions formation except for soot were predicted through this mechanism. The production and oxidation of soot mass was predicted using an empirical correlation developed by Hiroyasu et al. and is coupled with the Nagle and Strickland-Constable model [53, 54].

2.2. Boundary Conditions

The modeling strategy to use an extracted one-cylinder domain requires carefully selected boundary and initial conditions. As mentioned previously, a three-cylinder model was simulated for fifteen consecutive engine cycles until a quasi-steady state was reached in [28]. A monitoring volume was implemented in this model to compute the pressure, temperature, and species concentration at the inflow and outflow boundaries. These values were used as boundary conditions for the inlet and exhaust after being cycle-averaged. Additionally, flow variables were initialized using 3D data at exhaust port opening of the latest three-cylinder engine cycle that was simulated. Multiple engine cycles of the one-cylinder model were simulated given the nature of the LES turbulence modeling. This approach is validated in subsequent sections.

Wall heat transfer was predicted using the O'Rourke and Amsden model along with a standard wall function that uses the law-of-the-wall approximation to model the viscous sublayer [44]. Dirichlet temperature conditions were applied to wall boundaries and these values were supported through 1-D modeling of this OP-2S engine that was previously performed [17, 18, 19] and are listed in Table 2. The wall turbulent kinetic energy was prescribed as a Neumann boundary condition.

TABLE 2 Wall temperatures for various boundaries in the computational model

Intake Chest	320 K
Exhaust Chest	550 K
Cylinder Liner	400 K
Intake Piston	550 K
Exhaust Piston	550 K

2.3. Injection Parameters

The combustion chamber contains two wall-mounted injectors that are diametrically opposed and share a centerline. Each injector has three nozzles and are interdigitated such that the plumes are 60° out of phase with one another in order to avoid spray-to-spray interference, as illustrated by Figure 3. Table 3 lists the specifications of the injector that are relevant to the computational model. A CONVERGE predefined liquid (DIESEL2) was used to model the diesel liquid properties [29, 30,43]. The chemical kinetics sourced the evaporated gaseous diesel as n-heptane (C_7H_{16}). Evaporation data collected using this injector was used to prescribe a normalized rate-shape parameter for injection pressure and is shown in Figure 4.

2.4. Top-Land Model

It is crucial to model the top-land and piston-ring assembly in two-stroke engines to get accurate predictions of in-cylinder flows, heat transfer, and port opening/closing timings.

FIGURE 3 3D visualization of the two combustion chamber injectors, taken from data in this study.

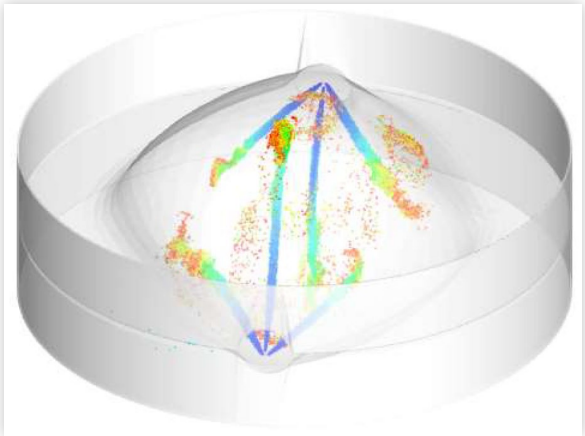

TABLE 3 Injector specifications for the Achates Power OP2S engine.

Discharge Coefficient	0.8
Nozzle Diameter	210 µm
Start of Injection (SOI)	9 CAD bMV
Injection Duration	14 CAD
Injected Mass per Injector	52.6 mg
Injected Fuel Temperature	355 K

FIGURE 4 Rate shape profile for injected pressure and velocity.

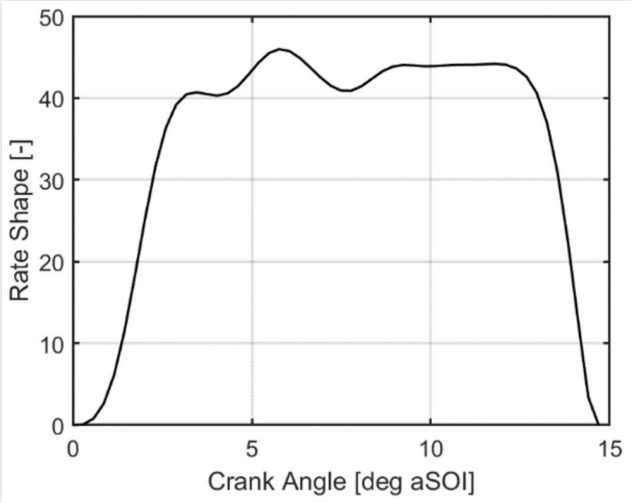

This work implements a top-land geometry on both the intake and exhaust pistons as shown in Figure 5a. More details on how the top-land height and clearance were determined through experimental analysis can be found in [28]. Figure 5b shows a comparison of the predicted cylinder pressure for simulations with and without a top-land model along with experimentally measured cylinder pressure. This cylinder pressure comparison demonstrates the need for a top-land geometry in this model.

2.5. Computational Grid and Verification

A base orthogonal grid of 1.6 mm was applied across the one-cylinder model domain but was refined using both fixed embedding and adaptive mesh refinement (AMR). Within the combustion chamber region, the grid was refined to 0.8 mm during the closed portion of the cycle. The grid was refined near the ports and along the combustion chamber walls (i.e., the cylinder liner, intake piston, and exhaust piston) to 0.4 mm. During the liquid spray process, embedding plumes for all six nozzles refined the grid further to 0.2 mm. AMR was used to refine the grid based on gradients of temperature, velocity, and liquid droplet fraction. The average minimum and maximum cell count for the simulations presented were 0.84 and 3.30 million cells, respectively.

LES turbulence modeling aims to resolve only the 'large', energy-containing eddies and model the sub-grid scale. Therefore, it is necessary to verify that the proposed grid is adequately modeling the sub-grid scale kinetic energy. A verification technique for 1-equation LES models was presented by Pope et al. by proposing a LES quality index [27]. LES quality ($Q(x,t)$) is defined as the ratio of the resolved turbulent kinetic energy ($K(x,t)$) to the total turbulent kinetic energy computed in both space and time, as defined in Equation 3. The resolved scale turbulent kinetic energy is defined in Equation 4, with the angled brackets representing the cycle-average.

$$Q(x,t) \equiv \frac{k_{res}(x,t)}{k_{res}(x,t) + k_{SGS}(x,t)} \tag{3}$$

$$k_{res}(x,t) = \frac{1}{2}\left\langle \left(U - \langle U \rangle\right) \cdot \left(U - \langle U \rangle\right) \right\rangle \tag{4}$$

$$\left\langle U(\theta) \right\rangle = \frac{1}{N_{cycles}} \sum_{l=1}^{N_{cycles}} U(\theta, l) \tag{5}$$

Using multiple cycles of this one-cylinder model, this quality metric was computed and analyzed using 3D data at two different points in the engine cycle: (a) at intake port closing (105 CAD bMV) and (b) prior to the liquid injection (10 CAD bMV). It should be noted that the intake port closing timing of 105 bMV considers the time at which the ring seals intake ports, which is different than the value shown in Table 1. Figure 6 plots a probability-density function (PDF) that illustrates the distribution of LES quality among the cells at these time steps. Previous work has indicated that an LES

FIGURE 5 (a) Top-land geometry shown for one of the pistons in the computational model. (b) Comparison of in-cylinder pressure for simulations with and without and top-land geometry as well as the experimental data for this operating condition.

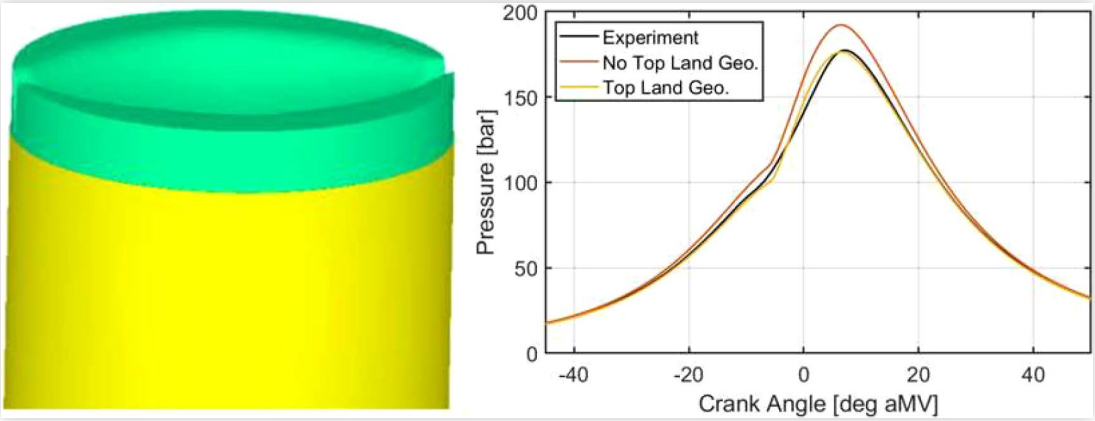

FIGURE 6 LES quality index (Q(x,t)) probability-density functions for data at two time steps: (a) Pre-spray (10 bMV) and (b) Intake Port Closing (105 bMV).

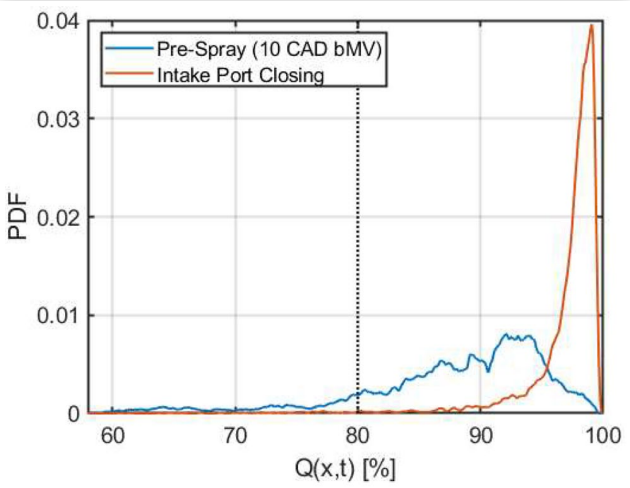

quality above 80% is considered to be 'good' such that the mesh structures contain at least 80% of the turbulent kinetic energy [24, 25, 26, 27]. The spatially averaged mean at intake port closing and prior to the liquid injection were found to be 97% and 85%, respectively. The tail end of both PDFs does indicate that there are regions where the LES quality index is lower. The pre-spray time step PDF even indicates some parts of the mesh below this threshold of 80% that typically lie near the wall and in the crevice created by the top-land model. With that said, it was determined that this level of LES quality index was sufficient verification of the computational grid.

2.6. Experimental Validation

A one-cylinder version of an Achates Power OP-2S engine was simulated for six consecutive engine cycles under the experimental operating conditions described in previous sections. Figure 7 plots the cycle-averaged cylinder pressure and gross heat release rates for: (a) experimentally measured data, (b) three-cylinder model using RANS (average of 11 cycles), and (c) one-cylinder model using LES (6 cycles). Three-cylinder results are presented here to illustrate how the one-cylinder LES model predicts heat release rates closer to those seen in the experiment. Previous work found the three-cylinder RANS predictions to be sufficient for studies of open-cycle performance [28].

FIGURE 7 Comparison of the cycle-averaged cylinder pressure and gross heat release rate for (a) experimentally measured data, (b) three-cylinder model using RANS turbulence modeling, and (c) one-cylinder model using LES.

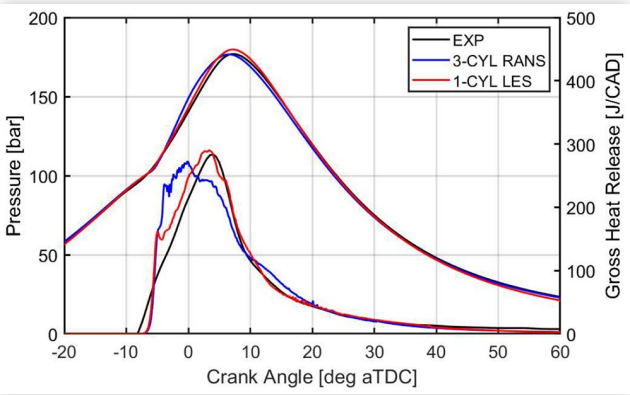

TABLE 4 Comparison of cycle-averaged performance parameters for the experimental operating point and the one-cylinder model simulations.

	One-Cylinder Model	Experiment
Delivered Mass [mg]	2936.6	2958.2
Trapped Mass [mg]	3520.1	3447.0
SR [-]	0.83	0.86
Bulk Swirl ratio [-]	2.491	-
Net IMEP [bar]	13.77	13.40
Soot Emissions [g/kW-hr]	0.038	0.015
NOx Emissions [g/kW-hr]	2.13	3.99
CO Emissions [g/kW-hr]	1.09	1.06
CO2 Emissions [g/kW-hr]	515.4	545.6
Ind. Thermal Efficiency [%]	47.85	48.60
CA50 [CAD aMV]	4.7	5.1
Burn Duration [CAD]	26.5	24.5

Table 4 lists performance parameters from the experimental data and the one-cylinder LES model simulations. Definitions of some parameters presented in this table are defined in a subsequent section. There is some difference for indicated thermal efficiency and net indicated mean effective pressure (IMEP) primarily due to the heat transfer predictions of the simulation. NOx and soot for the simulation also differ slightly but better agreement for these emissions predictions is generally considered difficult for CFD. With that said, there is a sufficient agreement between the experiment and simulation in terms of these performance parameters.

3. Performance Parameter Definitions

The following section defines some of the performance parameters used throughout this work. Scavenging parameters for two-stroke engines are defined via SAE J604 [47].

3.1. Scavenging Performance

Scavenging performance parameters quantify how well a two-stroke engine purges residual gases as well as retains fresh charge from the intake flow process. The scavenging ratio (SR) is defined as the ratio between the delivered mass through the intake and the mass trapped at port closing, as shown in Equation 7. At a SR > 1, the cylinder is considered to be over-scavenged while a SR < 1 is under-scavenged. Scavenging efficiency (SE) is the ratio between the delivered mass from the

intake that is retained in the cylinder to the mass trapped in the cylinder at port closing, shown in Equation 8. It is a measure of how well residuals from the previous cycle are purged out through the exhaust. Trapping efficiency (TE) defines the fraction of fresh charge that is retained in the cylinder as opposed to short circuited (SC) to the exhaust. It also is the ratio between scavenging efficiency and scavenging ratio, as defined in Equation 9. Delivery Ratio (DR) is defined as the ratio between the delivered mass through the intake and the theoretical mass of one displaced volume, defined in Equation 10.

$$SR = \frac{Delivered\ Mass}{Trapped\ Mass} \tag{7}$$

$$SE = \frac{Delivered\ Mass\ Retained}{Trapped\ Mass} \cdot 100 \tag{8}$$

$$TE = \frac{Delivered\ Mass\ Retained}{Delivered\ Mass} \cdot 100 = \frac{SE}{SR} = 1 - SC \tag{9}$$

$$DR = \frac{Delivered\ Mass}{Displaced\ Volume \cdot Ambient\ Density} \tag{10}$$

3.2. Vane Angle

Port vane angle is defined as the average of the angles created by the centerline of each port with the line connecting the center of the port to the bore center, as shown in Figure 8. This definition of port angle is used arbitrarily in this study to designate different port designs. The port designs were created by rotating the outer black ring relative to the inner black ring (in Figure 8) to induce more swirl through the intake ports. Figure 8 shows the largest port vane angle case while the other port designs are shown in the Appendix A1.

FIGURE 8 Graphical depiction of port vane angle (θ) definition used in this study.

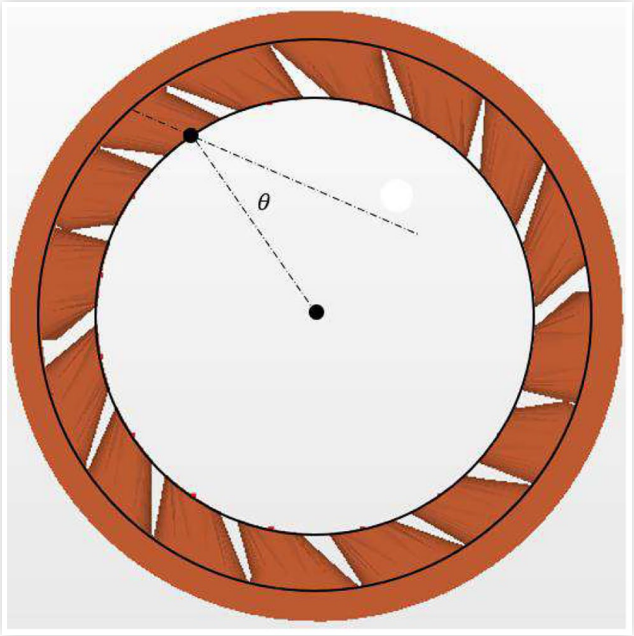

3.3. Swirl Ratio

Bulk swirl ratio in the combustion chamber is defined in Equation 11 as the ratio of the angular speed of flow around the z-axis (i.e., along the centerline of the cylinder) to the rotational speed of the crank shaft (1600 rpm for all cases in this study) [29, 30].

$$Swirl\ Ratio = \frac{\omega_z}{\omega_{crank}} \tag{11}$$

3.4. Cyclic Error

A sampling error formula was necessary in this study to quantify the cyclic variation seen for any performance parameter (θ). Cycle-to-cycle error for each case is defined in this study using a 95% confidence interval and student t-distribution, as shown in Equation 12. The units of the error are the same units of whichever performance parameter (θ) is listed. Cycle to cycle variation can also be quantified using the coefficient of variation which is defined as the ratio of the standard deviation to the mean of a given performance parameter (θ), shown in Equation 13.

$$Error = t_{0.95,N_{cycles}} \cdot \frac{\sigma_\theta}{\sqrt{N_{cycles}}} \tag{12}$$

$$COV = \frac{\sigma_\theta}{\mu_\theta} \cdot 100\% \tag{13}$$

4. Results

The one-cylinder OP-2S computational model described in previous sections was used to simulate five different intake port vane angle designs ranging from 12 degrees to 29 degrees for ten consecutive engine cycles. The first cycle of each simulation was initialized using 3D data from EPO on the three-cylinder model [28]. Boundary conditions for pressure, temperature, species fraction, and turbulent kinetic energy for flow boundaries and wall boundaries were also provided by cycle-averaged three-cylinder results and were kept constant for all cases of port vane angle. From a design perspective, the port vane angle is important to identify these designs but, for the purposes of this fundamental study, characterizing each case using the bulk swirl ratio at intake port closing is better suited.

Previous work analyzed the effects of swirl ratio and pressure difference on open cycle scavenging performance by only simulating the breathing stroke [28]. It was found that increasing bulk swirl ratio results in lower scavenging

TABLE 5 Bulk swirl ratio and trapped residual fraction at intake port closing (IPC) and its cyclic error for each case of port vane angle.

Port Vane Angle [degrees]	Bulk Swirl Ratio at IPC [-]	Trapped Residual Fraction [%]
12	1.360 ± 0.012	14.55 ± 0.38
19	2.597 ± 0.014	17.18 ± 0.32
23	2.998 ± 0.019	18.26 ± 0.29
26	3.353 ± 0.025	19.63 ± 0.21
29	3.718 ± 0.031	20.78 ± 0.25

FIGURE 9 Coefficient of variation for various performance parameters for each port design (defined by bulk swirl ratio).

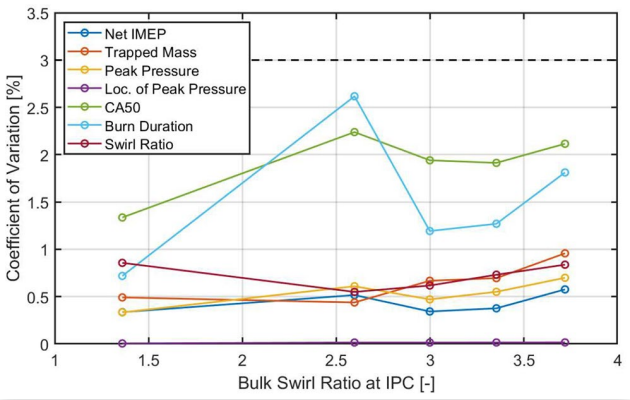

efficiency due to the larger angular momentum of the incoming intake flow that tends to concentrate a higher fraction of residuals along the cylinder centerline. Appendix A2 lists the open-cycle and closed-cycle performance parameters for the five port designs. These results indicate the same trends in open-cycle scavenging seen in previous work hold true when simulating multiple full engine cycles, further validating the previous approach to only simulate the breathing stroke. It is important to recognize that, although boundary conditions for these simulations are kept constant, the lower scavenging efficiency associated with larger port angles impacts the trapped charge composition across these cases.

Table 5 lists the bulk swirl ratio and trapped residual fraction at intake port closing with its cyclic error (defined in Section 3) for the five cases of port vane angle. Both parameters are relevant for characterizing the trapped conditions for the simulation space and there is shown to be relatively low cyclic variation for these parameters.

Simulation of LES turbulence modeling implores the use of convergence criteria ensuring mass flows, combustion performance, etc. have approached steady state. Figure 9 plots the coefficient of variation for various performance parameters for each port angle case defined by its bulk swirl ratio. Coefficient of variation (COV) is a statistical measure of the dispersion of samples about its mean. A threshold for this study was taken to be 3% as indicated by the black dashed line in Figure 9. For each performance parameter shown, it is below the maximum COV threshold. The CA50 and burn duration are higher than that of the other parameters which suggest slightly higher variability in the prediction of the heat release profile. Overall, the low variability provides confidence in using the cycle-averaged mean of each performance parameter to analyze trends with increasing swirl ratio. Throughout this section, performance parameters are presented as the cycle-averaged mean of ten cycles along with error bars for the cyclic error.

4.1. Pre-Spray Conditions

Figure 10 compares mass fraction of residuals cut planes for three port vane angle designs at 10 CAD bMV (1 CAD before start of injection [SOI]). These visualizations are shown as three cut planes: a horizontal plane parallel to the pistons along the injector centerlines, a vertical plane parallel to the pistons along the injector centerlines, and a vertical plane that is orthogonal to the other two. As shown in Table 5, the trapped residual fraction does increase for larger swirl ratios, but these cut-planes indicate that, prior to the spray, there is a higher concentration of residual mass in the center of the combustion chamber. Analysis of open-cycle results showed that higher swirl ratio tends to increase the concentration of hot residuals closer to the centerline of the combustion chamber at port closing [28]. Throughout the compression stroke, the piston bowl design acts to increase the level of swirl in the cylinder and thus keeps these residuals closer to the

FIGURE 10 Cut planes of residual mass fraction at 10 CAD bMV for three bulk swirl ratios: (a) 1.360, (b) 2.998, and (c) 3.718.

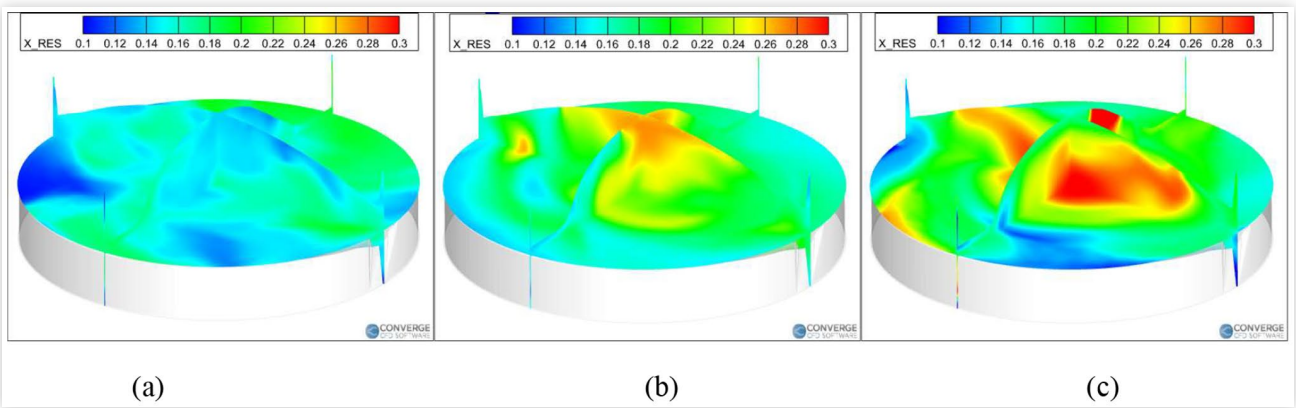

FIGURE 11 Normalized mean residual fraction and mean temperature at radial slices in the combustion chamber starting from the cylinder centerline (radial distance = 0) and extending to the liner walls.

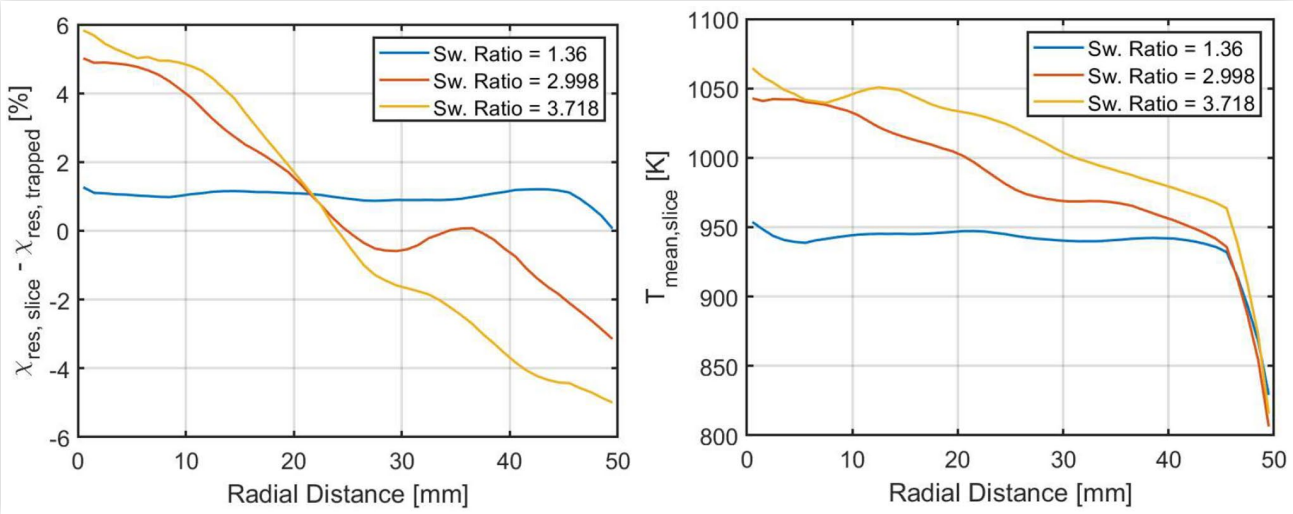

cylinder centerline. Figure 11 plots the mean residual fraction normalized by the trapped residual fraction and temperature at radial slices from the cylinder centerline (radial distance = 0) to the liner. At each slice, the amount of residuals was divided by the total mass then subtracted from the trapped residual fraction to accurately compare across these cases. For the low swirl ratio case, there is uniform distribution of the trapped residuals and cylinder temperature, excluding the boundary layer effects near the liner walls. As the swirl ratio increases and more residuals are forced to the center, the temperatures in the center of the combustion chamber also increase.

Figure 12 shows the mass-weighted probability density function of equivalence ratio and temperature for swirl ratio case at 10 CAD bMV. The equivalence ratio is calculated using the mole fraction of carbon, hydrogen, and oxygen for both the gas and liquid phases in the cell [29, 30]. The PDF is calculated prior to the spray such that the equivalence ratio is primarily dependent on the internal residuals and external exhaust gas recirculation (EGR) mass and not a function of injected fuel mass. As swirl ratio increases, both PDFs of equivalence ratio and temperature indicate that the mean value and breadth of the distribution increase. One of the reasons for this trend is due to the effect described in Figure 10 and 11 but it can also be attributed to the enhanced level of mixing as a result of more swirl. The combined effects on pre-spray equivalence ratio and temperature due to swirling fluid motion can have important implications for spray evaporation and emissions formation. More details and analysis on these effects are presented in later sections.

4.2. Combustion Performance

Figure 13 presents the indicated fuel efficiency, closed cycle heat loss, and burn duration as a function of swirl ratio.

FIGURE 12 Mass weighted-probability density functions for both equivalence ratio (a) and temperature (b) at 10 CAD bMV.

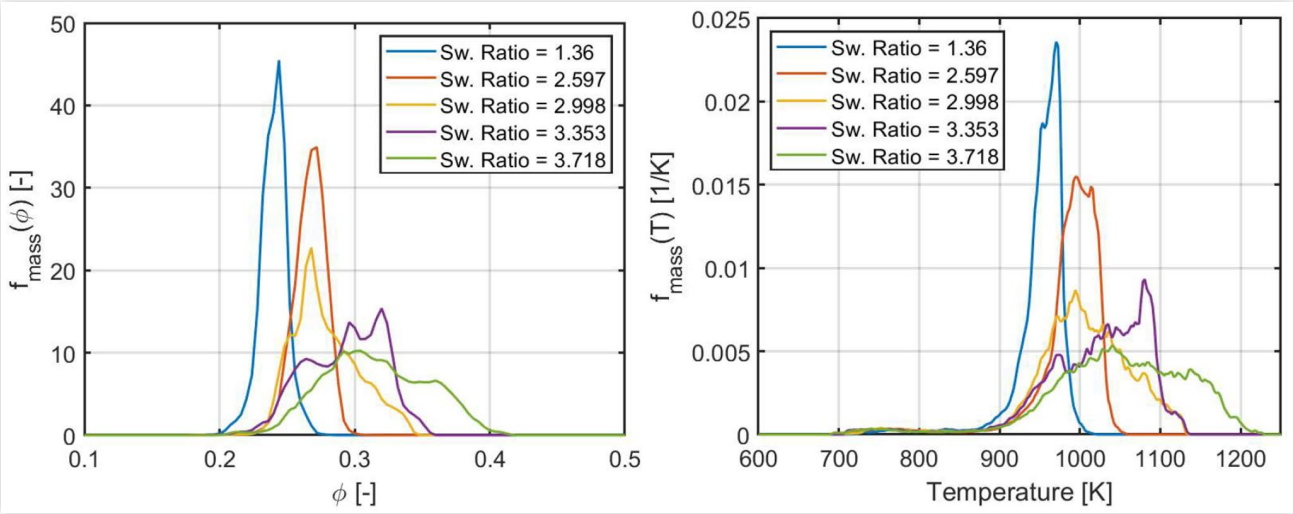

FIGURE 13 Indicated fuel efficiency, closed cycle heat loss, and burn duration plotted for each bulk swirl ratio case.

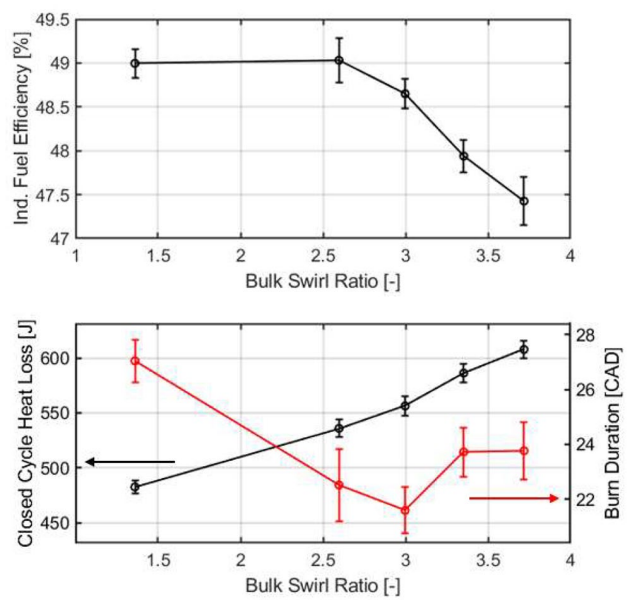

Swirling bulk motion of the fluid promotes advective heat transfer near the walls of the combustion chamber, thus explaining the fairly linear trend of closed cycle heat loss with bulk swirl ratio. In conjunction with this increased heat loss, more swirl shortens the burn duration. With not enough swirl, there is little mixing of the fuel-air mixture leading to a long burn duration. However, at this lowest swirl ratio, there is not as much heat lost. Increasing swirl ratio speeds up the burn duration to a point of diminishing returns while more heat is lost to the walls, resulting in a drop in fuel efficiency. This tradeoff between heat loss and burn duration indicates that there is a bulk swirl ratio above which no benefit in fuel efficiency is seen. From an open cycle scavenging perspective, there is a consistent benefit to scavenging efficiency with higher levels of swirl which conflicts with the trend seen in indicated fuel efficiency.

Figure 14 shows the tradeoff between NOx and soot emissions with increasing bulk swirl ratio. These emissions are computed by measuring the mass flow rate through the exhaust outflow boundary which does not consider the dynamic oxidation and agglomeration of soot in the cylinder through the expansion stroke. For the lowest bulk swirl ratio, there is the highest soot emissions and lowest NOx emissions. Production of NOx is typically correlated with higher in-cylinder temperatures, and, for this low swirl case, peak cylinder temperature is the lowest. Less mixing induced by swirling fluid flow tends to slow reaction rates and reduce cylinder temperatures, thus reducing NOx production. Additionally, the slower reaction rates and later combustion phasing along with less mixing produces the highest levels of soot. With increasing swirl, higher in-cylinder temperatures and enhanced fuel-air mixing result in more NOx emissions and less soot emissions. It is important to note that there is larger cyclic variability associated with these emissions values that makes it hard to discern differences between the two highest swirl ratio cases.

FIGURE 14 Indicated specific NOx and soot emissions for each bulk swirl ratio case.

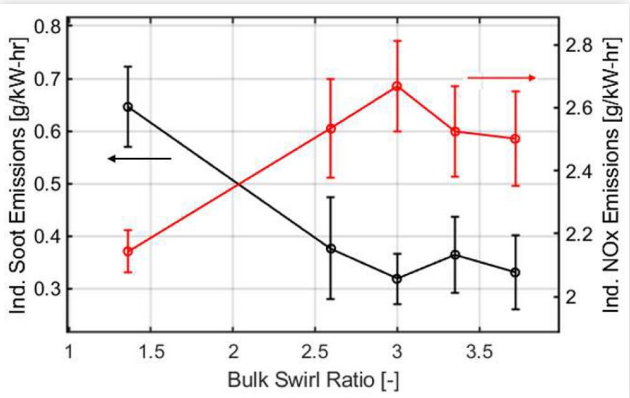

4.3. In-Cylinder Distributions

Figure 12 above presents the mass-weighted probability density functions for both equivalence ratio and temperature at a point prior to the injection of the spray. However, during and after the liquid fuel injection process, the evaporation and subsequent ignition of the fuel creates a coupling between equivalence ratio and temperature that cannot be accurately represented with a one-dimensional PDF. Instead, the use of a mass-weighted joint probability density function (jPDF) is warranted to visualize the diesel combustion process and its effect on performance and emissions. Figure 15 shows two joint probability density functions based on equivalence ratio and temperature for the 19-degree port angle design at 0 CAD aMV (during the spray) and 14 CAD aMV (post-spray). The jPDFs are weighted by the fuel mass in each computational cell instead of total mass to highlight the fuel distribution. During the spray, there is still fuel mass at high equivalence ratios that has yet to fully mix but after the spray and during combustion, this fuel mass has mixed down to lower equivalence ratio regions (e.g., leaner regions due to mixing and entrainment of air). The adiabatic flame temperature for this fuel peaks at an equivalence ratio that is slightly rich which explains the 'boomerang' shape of distribution. Previous work has used a similar plot to show the soot and NOx islands for diesel fuel [52]. These jPDFs have the powerful ability to show the density of fuel mass in ranges of equivalence ratio and temperature that could form NOx and soot.

Figure 16a-b compares the fuel mass-weighted jPDFs at 14 CAD aMV for two port angle designs: (a) 12 degrees and (b) 29 degrees. Figure 16c plots a jPDF difference map that is the result of subtracting the jPDF in Figure 16a from the one in Figure 16b. The regions colored red indicate more mass in that region for the higher swirl case and conversely, the blue regions have more mass for the lower swirl case. With the lower swirl case, there is still mass at higher equivalence ratio (greater than 2) that has not mixed enough with the cylinder charge. Higher levels of swirl enhance the fuel-air mixing which is evident in the higher density of mass between an equivalence ratio of about 0.7 to 2. At low

FIGURE 15 Fuel mass-weighted joint probability density function based on equivalence ratio and temperature for the 19-degree port angle design at (a) 0 CAD a MV and (b) 14 CAD aMV.

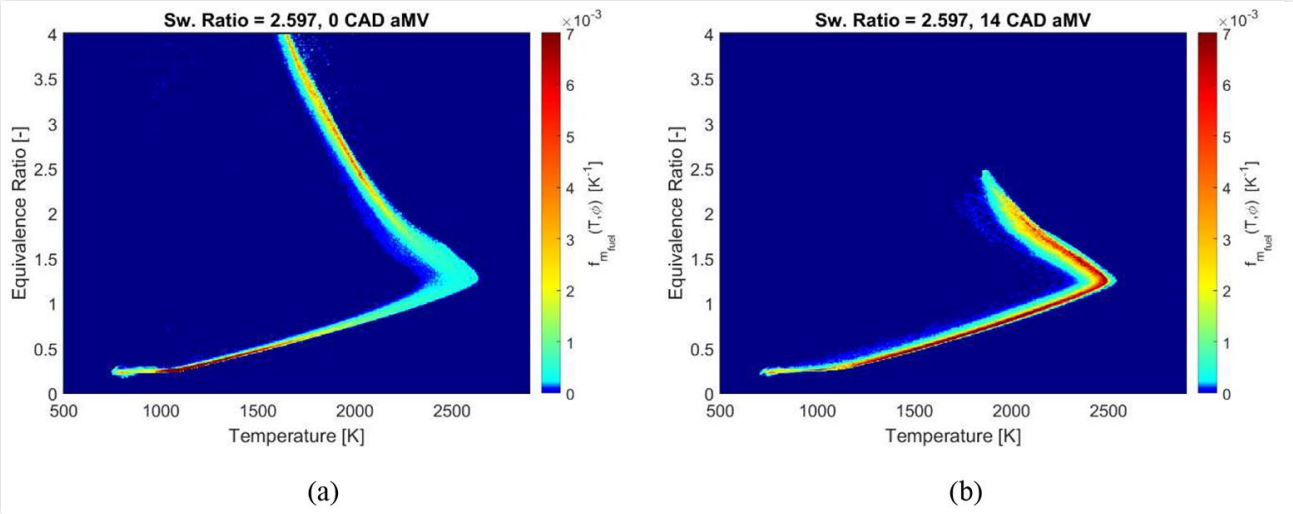

FIGURE 16 Fuel mass-weighted joint probability density functions at 14 CAD aMV for two port angle designs: (a) 12 degrees (Sw. Ratio = 1.360) and (b) 29 degrees (Sw. Ratio =3.718). (c) Joint probability density function difference map for these two cases.

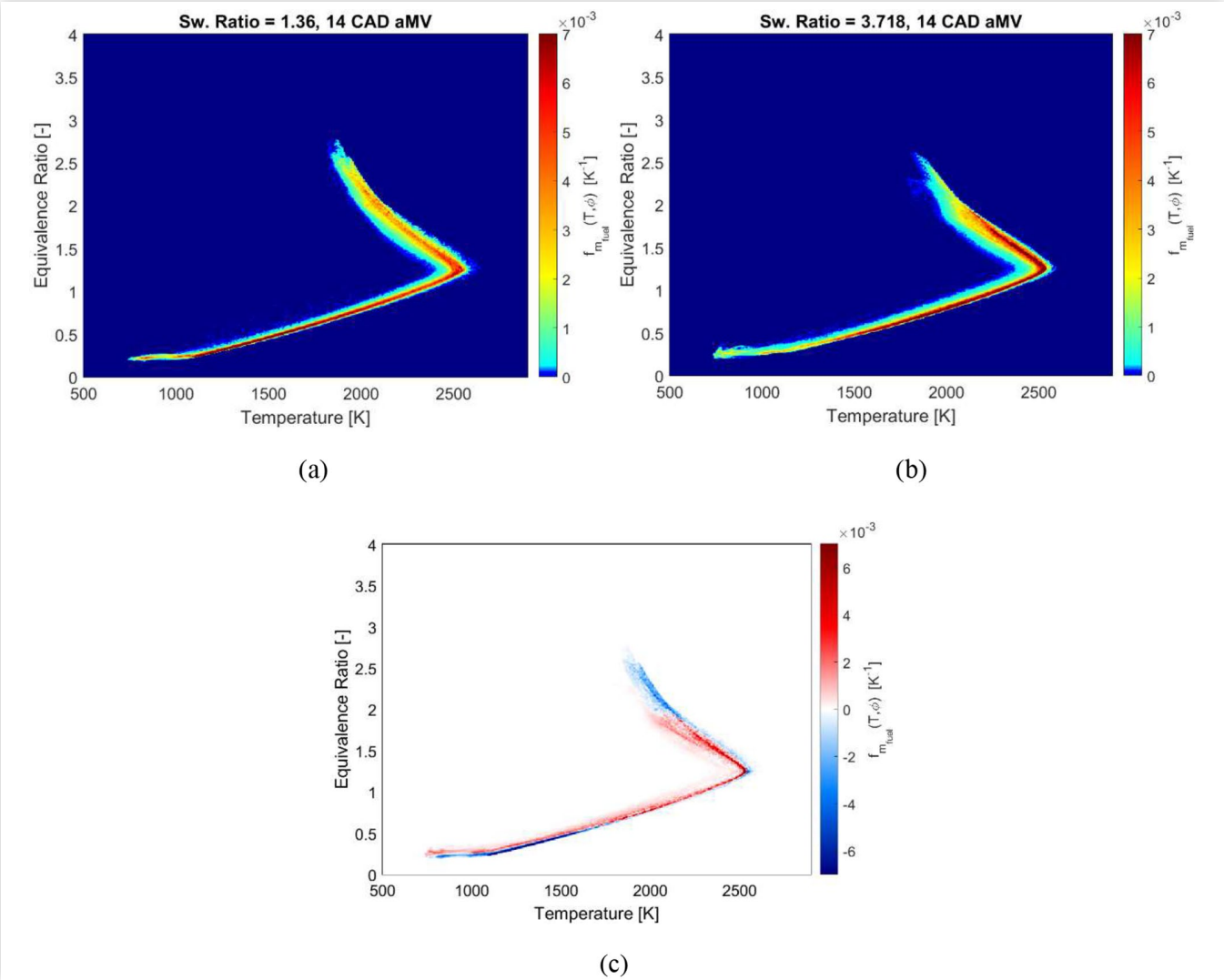

FIGURE 17 Joint probability density function difference maps based on equivalence ratio and temperature weighted by (a) soot mass and (b) NOx mass for the highest and lowest swirl cases. Regions colored red are where a higher density of the higher swirl case is evident, while blue colored regions represent a higher mass density in the lower swirl case.

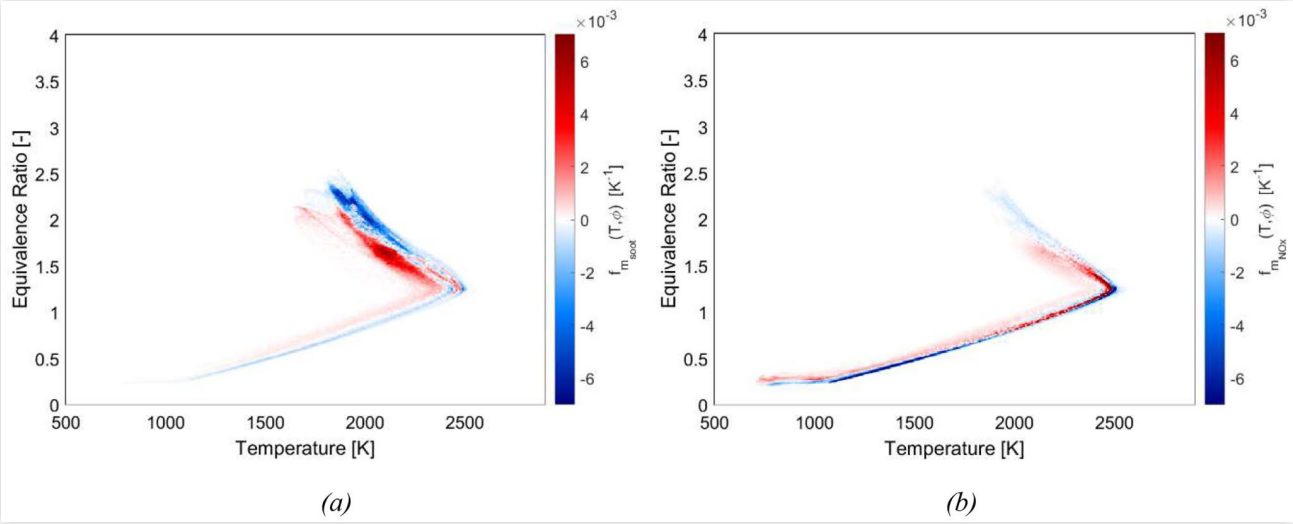

equivalence ratios, the distributions diverge due to differences in trapped residual fraction and pre-spray distributions, as seen in Figure 12.

Soot and NOx contours for diesel fuel could be interpolated onto the jPDFs shown in Figure 16 to give an indication of the emissions formation regions. A different approach was used in this study by utilizing a difference map between jPDFs that are weighted by soot and NOx mass instead of fuel or total mass. Figure 17 presents the jPDF difference maps based on (a) soot and (b) NOx for the highest and lowest swirl cases at 14 CAD aMV. The soot mass jPDF difference map indicates that the highest density lies in the range of a high equivalence ratio and at temperatures less than the peak cylinder temperature. The NOx mass jPDF difference map shows higher density at the leaner regions of the cylinder and near the peak cylinder temperature. The port design with lower swirl contains a higher fraction of rich regions that are at lower temperatures and produce more soot. Increasing the swirl ratio mixes these richer regions to lower equivalence ratios that are closer to the peak adiabatic flame temperature, and thus produce less soot but more NOx.

4.4. Visualizing Emissions Formation

Figure 18 shows iso-surfaces of soot and NOx mass for the two port design cases with the highest and lowest bulk swirl ratio at 6 CAD aMV (1 CAD after end of injection). The injector configuration and piston bowl design used in this study produces spray plumes that direct part of the fuel at the piston. The soot iso-surfaces indicate high density regions that are at end of these spray plumes near the walls of the piston. Any fuel that rebounds off the piston loses more heat to the piston walls, which reduces the temperature in these regions. Consequently, these low temperature, high soot regions have the least NOx mass. NOx mass iso-surfaces have a generally uniform distribution in both cases of swirl ratio but only in regions near the center of the cylinder. This result agrees with the pre-spray gradient of temperature over the radial distance that was shown previously in Figure 12. As the swirl is increased, there is less soot and more NOx produced which is evident in the differences between the iso-surfaces. The high-density islands of soot mass are seen to be smaller and distorted by the enhanced swirling motion. Additionally, the NOx region in the higher swirl case is still in the center of the cylinder but the effective volume has grown. These iso-surfaces provide a qualitative understanding of the regions where soot and NOx are formed that are heavily dependent on the injector configuration.

There exists an optimum level of swirl that both maximizes fuel efficiency, emissions output, and open-cycle scavenging performance. Ultimately, that optimum swirl level is most likely slightly less than that of the 19-degree port angle case (bulk swirl ratio of 2.597). As shown previously, there is a steep decrease in fuel efficiency associated with swirl levels higher than this case, but, the NOx emissions for this port design are much higher than that of the lowest swirl case. If lower NOx is desired without a fuel efficiency penalty, a shallower port angle design might be necessary which would adversely impact the scavenging performance. Instead, an alternative approach could be to modify the injector configuration to optimize the combustion performance at this swirl ratio. Future work using a similar computational methodology could investigate these spray design parameters to reduce harmful soot and NOx emissions.

5. Conclusions

A one-cylinder computational model of an OP-2S was simulated using Large Eddy Simulations and validated to data collected at a high brake thermal efficiency experimental

FIGURE 18 Iso-surfaces of Soot and NOx mass for lowest and highest swirl ratio port designs at 6 CAD aMV

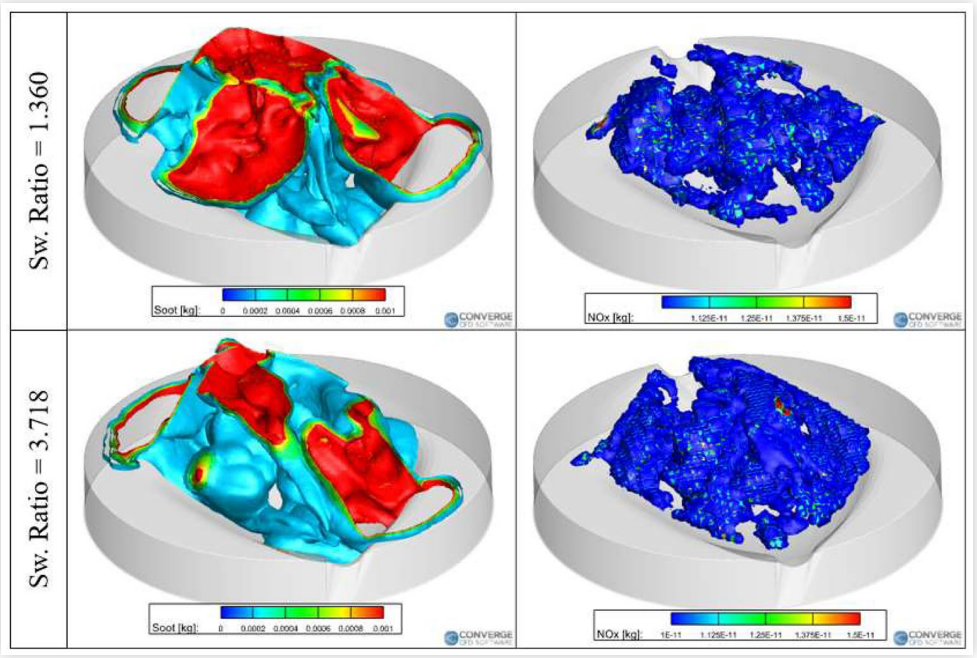

operating condition [18, 19]. This model was used to simulate five cases of port designs with varying bulk swirl ratios for ten consecutive engine cycles and was used to analyze the closed cycle performance of each design. The following conclusions can be drawn from this work:

- A computational model using LES turbulence modeling that accurately represents flow conditions seen in the Achates Power OP-2S was developed and validated. This model presents future opportunities to investigate other parameters in this OP-2S design.
- Increasing bulk swirl ratio concentrates a larger fraction of internal residuals closer to the centerline of the combustion chamber which results in a broader distribution of in-cylinder equivalence ratio and temperature prior to the injection of the diesel fuel.
- Indicated fuel efficiency suffers with swirl ratios higher than a certain threshold due to competing effects associated with heat loss and burn duration.
- With lower swirl ratios, there is less mixing of rich regions of fuel that contribute to higher levels of soot emissions. Conversely, increasing swirl ratio mixes these rich regions into ranges of lower equivalence ratios (near stoichiometry) that produce higher temperatures associated with greater NOx emissions.
- Analysis of the locations within the cylinder that produce soot and NOx emissions suggests the current spray configuration is not optimized. Future work could investigate certain injection parameters to reduce regions near the wall that generate soot and high temperature regions that produce NOx.

The conclusions drawn above are critical to opposed-piston two-stroke engine operation. However, trends in scavenging performance can be applied to a wider subset of two-stroke engines not limited to the opposed-piston design. Additionally, the computational strategy for analyzing open-cycle and closed-cycle presents value for the engine community at large.

References

1. Kalka, J., Opaliński, M., and Szczeciński, M., "Opposed-Piston Engines: the Future of Internal Combustion Engines," *PhD Interdisciplinary Journal* 1 (2014).
2. Endicott, D.L. and Tervo, W.J., "Combustion Chamber Design for Two-Stroke Cross-Flow Outboard Engines," SAE Technical Paper 620170, 1962, 10.4271/620170.
3. Bajwa, A.U., Patterson, M., and Jacobs, T.J., "Using Gas Dynamic Models to Improve Exhaust System Design for Large-Bore, Two-Stroke Engines," *International Journal of Engine Research* 22, no. 8 (2021): 2622-2638.
4. Dang, D. and Wallace, F.J., "Some Single Zone Scavenging Models for Two-Stroke Engines," *International Journal of Mechanical Sciences* 34, no. 8 (1992): 595-604.
5. Xu, Z., Ji, F., Ding, S., Zhao, Y. et al., "Simulation and Experimental Investigation of Swirl-Loop Scavenging in Two-Stroke Diesel Engine with Two Poppet Valves," *International Journal of Engine Research* 22, no. 6 (2021): 2021-2034.
6. Sammons, H., "A Single-Cycle Test Apparatus for Studying "Loop Scavenging" in a Two-Stroke Engine," *Proceedings of the Institution of Mechanical Engineers* 161, no. 1 (1949): 233-249.
7. Blair, G.P., Kenny, R.G., Smyth, J.G., Sweeney, M.E.G. et al., "An Experimental Comparison of Loop and Cross

Scavenging of the Two-Stroke Cycle Engine," *SAE Transactions* (1986): 1040-1050.

8. Mitianiec, W., "Analysis of Loop Scavenging Process in a Small Power SI Two-Stroke Engine," *SAE Transactions* (2002): 2439-2448.
9. Zhu, Q., Yuan, Z.C., Guo, W.C., and Yu, Y.X., "Numerical Simulation of Gas Exchange Process in Two Stroke Reverse-Loop Scavenging Engines," in: , *Advanced Materials Research*. Vol. 468, (Trans Tech Publications Ltd, 2012), 2259-2264.
10. Laget, O., Ternel, C., Thiriot, J., Charmasson, S. et al., "Preliminary Design of a Two-Stroke Uniflow Diesel Engine for Passenger Car," *SAE International Journal of Engines* 6, no. 1 (2013): 596-613.
11. Ingvorsen, K.M., Meyer, K.E., Walther, J.H., and Mayer, S., "Turbulent Swirling Flow in a Model of a Uniflow-Scavenged Two-Stroke Engine," *Experiments in Fluids* 54, no. 3 (2013): 1-17.
12. Wang, X. and Zhao, H., "Effect of Piston Shape Design on the Scavenging Performance and Mixture Preparation in a Two-Stroke Boosted Uniflow Scavenged Direct Injection Gasoline Engine," *International Journal of Engine Research* 22, no. 5 (2021): 1484-1499.
13. Blair, G.P., *Design and Simulation of Two-Stroke Engines* (Warrendale, PA: Society of Automotive Engineers, 1996), 472-511.
14. Blair, G.P., *Two-Stroke Engines* (Society of Automobile Engineering, 1990)
15. Johnson, D., Wahl, M., Redon, F., Dion, E. et al., "Opposed-Piston Two-Stroke Diesel Engine-A Renaissance," in *Symposium on International Automotive Technology (SIAT)*, 2011, January, 1.
16. Regner, G., Herold, R.E., Wahl, M.H., Dion, E. et al., "The Achates Power Opposed-Piston Two-Stroke Engine: Performance and Emissions Results in a Medium-Duty Application," *SAE International Journal of Engines* 4, no. 3 (2011): 2726-2735.
17. Herold, R.E., Wahl, M.H., Regner, G., Lemke, J.U. et al., "Thermodynamic Benefits of Opposed-Piston Two-Stroke Engines," SAE Technical Paper 2011-01-2216, 2011, 10.4271/2011-01-2216.
18. Redon, F., Sharma, A., and Headley, J., "Multi-Cylinder Opposed Piston Transient and Exhaust Temperature Management Test Results," SAE Technical Paper 2015-01-1251, 2015, 10.4271/2015-01-1251.
19. Sharma, A. and Redon, F., "Multi-Cylinder Opposed-Piston Engine Results on Transient Test Cycle," SAE Technical Paper 2016-01-1019, 2016, 10.4271/2016-01-1019.
20. Chown, D., Koszewnik, J., MacKenzie, R., Pfeifer, D. et al., "Achieving Ultra-Low Oil Consumption in Opposed Piston Two-Stroke Engines," SAE Technical Paper 2019-01-0068, 2019, 10.4271/2019-01-0068.
21. Nagar, N., Sharma, A., Redon, F., Sukumar, B. et al., "Simulation and Analysis of After-Treatment Systems (ATS) for Opposed-Piston 2 Stroke Engine," in *Emissions 2016 Conference*, 2016.
22. Nagar, N., Sharma, A., Redon, F., Sukumar, B. et al., "Simulation and Analysis of After-Treatment Systems (ATS) for Opposed-Piston 2 Stroke Engine," in *Emissions 2016 Conference*, 2016.
23. d'Adamo, A., Breda, S., Fontanesi, S., and Cantore, G., "A RANS-Based CFD Model to Predict the Statistical Occurrence of Knock in Spark-Ignition Engines," *SAE International Journal of Engines* 9, no. 1 (2016): 618-630.
24. Rutland, C.J., "Large-Eddy Simulations for Internal Combustion Engines-a Review," *International Journal of Engine Research* 12, no. 5 (2011): 421-451.
25. Lee, D., Pomraning, E., and Rutland, C.J., "LES Modeling of Diesel Engines," *SAE Transactions* (2002): 2566-2578.
26. Mittal, V., Kang, S., Doran, E., Cook, D. et al., "LES of Gas Exchange in IC Engines," *Oil & Gas Science and Technology-Revue d'IFP Energies Nouvelles* 69, no. 1 (2014): 29-40.
27. Celik, I., Yavuz, I., and Smirnov, A., "Large Eddy Simulations of In-Cylinder Turbulence for Internal Combustion Engines: A Review," *International Journal of Engine Research* 2, no. 2 (2001): 119-148.
28. O'Donnell, P.C., Gandolfo, J., Gainey, B., Vorwerk, E. et al., "Effects of Port Angle on Scavenging of an Opposed Piston 2-Stroke Engine," SAE Technical Paper 2022-01-0590, 2022, 10.4271/2022-01-0590.
29. Richards, K.J., Senecal, P.K., and Pomraning, E., *Converge 3.0* (Madison, WI: Convergent Science, 2019)
30. Richards, K.J., Senecal, P.K., and Pomraning, E., *Converge 3.0 Manual* (Madison, WI: Convergent Science, 2019)
31. Soave, G., "Equilibrium Constants from a Modified Redlich-Kwong Equation of State," *Chemical Engineering Science* 27, no. 6 (1972): 1197-1203.
32. Oliveira, J., Raad, I., and Issa, P., "An Improved PISO Algorithm for the Computation of Buoyancy-Driven Flows," *Numerical Heat Transfer, Part B: Fundamentals* 40, no. 6 (2001): 473-493.
33. Wang, T., Gu, C.G., Yang, B., and Huang, J.G., "PISO Algorithm for Unsteady Flow Field," *Journal of Hydrodynamics* 18, no. 2 (2003): 233-239.
34. Amsden, A.A., O'Rourke, P.J., and Butler, T.D., "KIVA-II: A Computer Program for Chemically Reactive Flows with Sprays," Los Alamos National Laboratory Technical Report LA-11560-MS, 1989.
35. Reitz, R.D. and Bracco, F.V., "Mechanisms of Breakup of Round Liquid Jets," Encyclopedia.
36. Reitz, R.D., "Modeling Atomization Processes in High-Pressure Vaporizing Sprays".
37. Reitz, R.D. and Diwakar, R., "Structure of High-Pressure Fuel Sprays," SAE Technical Paper 870598, 1987, 10.4271/870598.
38. Liu, A.B., Mather, D.K., and Reitz, R.D., "Modeling the Effects of Drop Drag and Breakup".
39. Schmidt, D.P. and Rutland, C.J., "A New Droplet Collision Algorithm," Journal of.
40. Senecal, P.K., Pomraning, E., and Richards, K.J., "Multi-Dimensional Modeling of DirectInjection Diesel Spray Liquid Length and Flame Lift-Off Length using CFD and Parallel Detailed Chemistry," SAE Technical Paper 2003-01-1043, 2003, 10.4271/2003-01-1043.

41. Lawrence Livermore National Laboratory, SUNDIALS, https://computation.llnl.gov/casc/sundials/main.html, Accessed July 2015.
42. Turns, S.R., *An Introduction to Combustion* (McGraw-Hill, Inc., 1996)
43. Golovitchev, V.I., http://www.tfd.chalmers.se/~valeri/MECH.html, Chalmers Univ of Tech, Gothenburg, Sweden, 2000.
44. Angelberger, C., Poinsot, T., and Delhaye, B., "Improving Near-Wall Combustion and Wall Heat Transfer Modeling in SI Engines Computations," SAE Technical Paper 972881, 1997, 10.4271/972881.
45. Blair, G.P., *Design and Simulation of Two-Stroke Engines* (Warrendale, PA: Society of Automotive Engineers, 1996), 472-511.
46. Blair, G.P., *Two-Stroke Engines* (Society of Automobile Engineering, 1990)
47. J604_199506, SAE IC Powertrain Steering Committee, Engine Terminology and Nomenclature-General, June 1995, https://doi.org/10.4271/J604_199506.
48. Gafoor, C.A. and Gupta, R., "Numerical Investigation of Piston Bowl Geometry and Swirl Ratio on Emission from Diesel Engines," *Energy Conversion and Management* 101 (2015): 541-551.
49. Wei, S., Wang, F., Leng, X., Liu, X. et al., "Numerical Analysis on the Effect of Swirl Ratios on Swirl Chamber Combustion System of DI Diesel Engines," *Energy Conversion and Management* 75 (2013): 184-190.
50. Kook, S., Bae, C., Miles, P.C., Choi, D. et al., "The Effect of Swirl Ratio and Fuel Injection Parameters on CO Emission and Fuel Conversion Efficiency for High-Dilution, Low-Temperature Combustion in an Automotive Diesel Engine," *SAE Transactions* (2006): 111-132.
51. Shi, Y. and Reitz, R.D., "Optimization Study of the Effects of Bowl Geometry, Spray Targeting, and Swirl Ratio for a Heavy-Duty Diesel Engine Operated at Low and High Load," *International Journal of Engine Research* 9, no. 4 (2008): 325-346.
52. Dhal, G.C., Mohan, D., and Prasad, R., "Preparation and Application of Effective Different Catalysts for Simultaneous Control of Diesel Soot and NOX Emissions: An Overview," *Catalysis Science & Technology* 7, no. 9 (2017): 1803-1825, doi:10.1039/C6CY02612E.
53. Nagle, J. and Strickland-Constable, R.F., "Oxidation of Carbon Between 1000-2000 C," in *Proceedings of the Fifth Carbon Conference*, 1962, 1, Pergammon Press.
54. Hiroyasu, H. and Kadota, T., "Models for Combustion and Formation of Nitric Oxide and Soot in DI Diesel Engines," SAE Technical Paper 760129, 1976, 10.4271/760129.

Contact Information

Patrick C. O'Donnell,
odonne9@clemson.edu

Acknowledgements

This work was supported by the Department of Energy's Vehicle Technologies Office under award number DE-EE0009202. The authors would gratefully like to acknowledge Clemson University's Cyberinfrastructure Technology Integration (CITI) group for providing ample computational resources through the Palmetto supercomputing cluster, as well as CONVERGE for providing access to their CFD software.

Appendix

APPENDIX A1 Simulated port designs in the one-cylinder model for vane angles of 12° (a), 19° (b), 23° (c), 26° (d), and 29° (d).

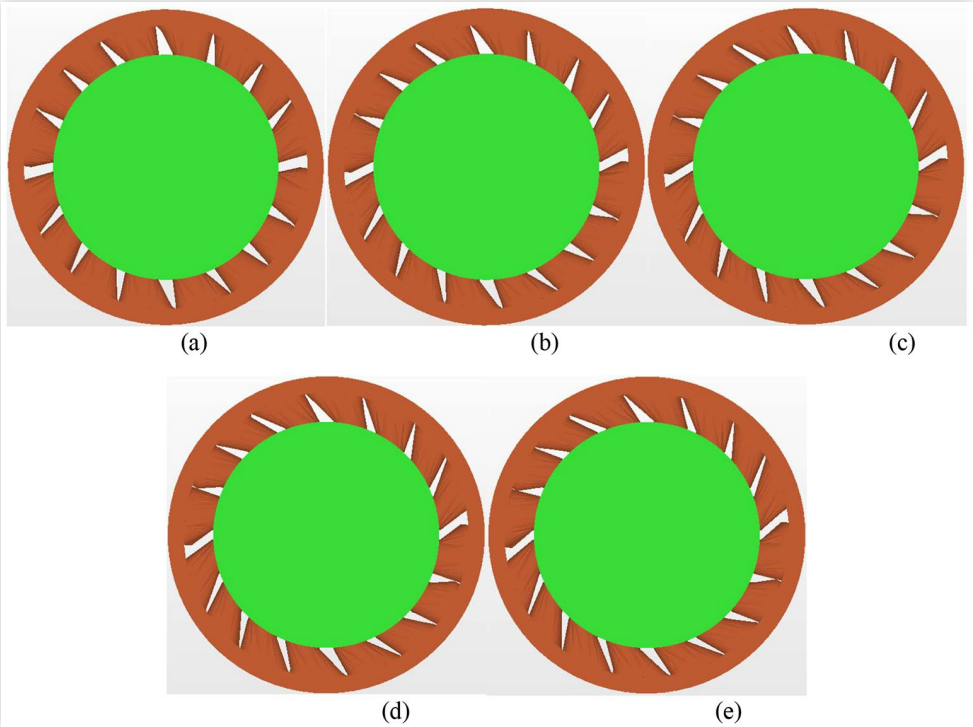

APPENDIX A2 Cycle-averaged performance parameters for the five port designs simulated in this study.

Port Angle	*12 deg.*	*19 deg.*	*23 deg.*	*26 deg.*	*29 deg.*
Delivered Mass [mg]	3501.0	3235.1	3114.5	2963.7	2836.5
Trapped Air Mass [mg]	3558.2	3394.4	3276.0	3156.8	3036.9
Trapped Mass [mg]	3773.5	3618.7	3505.4	3392.8	3279.1
SR [-]	0.93	0.89	0.89	0.87	0.87
SE [%]	85.45	82.82	81.74	80.37	79.22
TE [%]	92.10	92.64	92.00	92.01	91.57
Residual Fraction [%]	14.55	17.18	18.26	19.63	20.78
Bulk Swirl ratio [-]	-1.360	-2.597	-2.998	-3.353	-3.718
Closed Cycle Heat Transfer [J]	482.5	535.9	556.4	586.4	607.8
Net IMEP [bar]	14.07	14.08	13.97	13.76	13.62
Indicated Thermal Efficiency [%]	49.00	49.03	48.65	47.94	47.43
CA50 [CAD aMV]	5.27	4.55	4.48	4.58	4.52
Burn Duration [CAD]	27.05	22.52	21.59	23.73	23.77
Peak Pressure [bar]	183.3	186.2	185.1	182.4	181.0
Peak Temperature [K]	1680.3	1781.4	1828.7	1851.5	1887.6
Soot Emissions [g/kW-hr]	0.65	0.38	0.32	0.36	0.33
NOx Emissions [g/kW-hr]	2.14	2.53	2.67	2.52	2.50
CO Emissions [g/kW-hr]	1.15	0.42	0.41	0.42	0.54
CO2 Emissions [g/kW-hr]	504.4	505.2	509.2	516.8	522.2

ISSN 0148-7191